Electronic Properties of Isosymmetric Phase Boundaries in Highly Strained Ca-Doped $BiFeO_3$

Jan Seidel, Morgan Trassin, Yi Zhang, Peter Maksymovych, Tino Uhlig, Peter Milde, Denny Köhler, Arthur P. Baddorf, Sergei V. Kalinin, Lukas M. Eng, Xiaoqing Pan, and Ramamoorthy Ramesh*

Interfaces in complex oxide materials are currently receiving increased interest in condensed matter science.[1–5] Engineered interfaces created through heteroepitaxy are a key focal point,[2,4,5] while "natural" interfaces such as domain walls draw considerable attention as well.[6–14] As a prominent example, the complex oxide $BiFeO_3$ (BFO) has been shown to host several interesting aspects brought about by domain walls and has generated interest across many scientific disciplines.[15–21] Promising concepts of BFO nanoscale domain and domain wall engineering through strain and doping have been demonstrated recently, including the fabrication of the nearly tetragonal (T) variant of BFO.[22–25] Remarkably, this T structural phase has an extremely large c/a ratio of around 1.25 achieved through substrate strain on $LaAlO_3$ (LAO) (4.5% lattice mismatch). Due to the high in-plane compressive strain a large expansion of the out-of-plane lattice parameter is observed. Epitaxial stabilization of the T-phase is of significant interest as it has a high polarization value of over 150 μC cm^{-2}, which is about 50% higher than its rhombohedral (R) counterpart.[26] BFO films grown on LAO substrates show a mixed T- and R-phase character with the relative fraction dependent on the film thickness. In these films needle-shaped R domains are embedded into a T-phase matrix, with the ability to selectively switch between the two phases by application of electric fields.[23] This R–T phase mixture exhibits a giant piezoelectric coefficient, enabled by phase boundary motion.[23] The finding of a strain-stabilized isosymmetric phase boundary in this multiferroic compound is unusual, resulting in strong interest in this system and considerable prospects for new phenomena. The strain induced transition between crystallographically equivalent (isosymmetric) structures offers a new landscape for tailoring highly anisotropic electronic responses in complex oxides. The fundamental understanding of electronic properties of such boundaries presents a very interesting new aspect of oxide interface functionality after electronic properties of ferroelectric domain walls as "natural" oxide interfaces have recently received considerable interest.[27–34] Here, we demonstrate anisotropic electronic conductivity of isosymmetric phase boundaries in BFO, which are the (fully epitaxial) connecting regions between two different structural variants of the same material, including its coupling to the phase transformation. For this, we employ a combination of temperature dependent conductive atomic force microscopy (c-AFM) with high angle annular dark field (HAADF) imaging and electron energy loss spectroscopy (EELS) using spherical aberration-corrected scanning transmission electron microscopy (STEM). Strong correlations between nanoscale phase transition and local electronic conductivity are found. We further demonstrate that a high degree of control over the electronic properties of the phase boundaries can be attained through non-local electrical switching.

Strain relaxation through control of the BFO film thickness allows control of the fraction of T and R phase mixture. In our case the growth of 80 nm thick films of BFO doped with 2% Ca result in the mixed phase morphology shown in **Figure 1**a as imaged by atomic force microscope (AFM). The individual stripe-like regions with a length of ≈500 nm and a width of 50–100 nm are the R-phase regions, which are visible with high resolution in the deflection signal (Figure 1b). Figure 1c shows the local conductivity of the same region measured by c-AFM. Interestingly the phase boundaries appear as conductive lines. The graph in Figure 1d shows a cross-sectional line-profile of the mixed phase area (see cut in Figure 1c),

Dr. J. Seidel
School of Materials Science and Engineering
University of New South Wales
Sydney, NSW 2052, Australia
E-mail: jan.seidel@unsw.edu.au
Dr. J. Seidel, Prof. R. Ramesh
Materials Sciences Division
Lawrence Berkeley National Laboratory
Berkeley, CA 94720, USA
Dr. J. Seidel, Prof. R. Ramesh
Department of Physics
University of California, Berkeley
Berkeley, CA 94720, USA
Dr. M. Trassin, Prof. R. Ramesh
Department of Materials Science and Engineering
University of California, Berkeley
Berkeley, CA 94720, USA
Dr. M. Trassin
Department of Materials
ETH Zurich
Wolfgang-Pauli-Strasse 10, 8093, Zurich, Switzerland
Dr. Y. Zhang, Prof. X. Pan
Department of Materials Science and Engineering
University of Michigan
Ann Arbor, MI 48109, USA
Dr. P. Maksymovych, Dr. A. P. Baddorf, Dr. S. V. Kalinin
Center for Nanophase Materials Science
Oak Ridge National Laboratory
Oak Ridge, TN 37831, USA
Dr. T. Uhlig, Dr. P. Milde, Dr. D. Köhler, Prof. L. M. Eng
Institute of Applied Photophysics
Technische Universität Dresden
01062 Dresden, Germany

DOI: 10.1002/adma.201400557

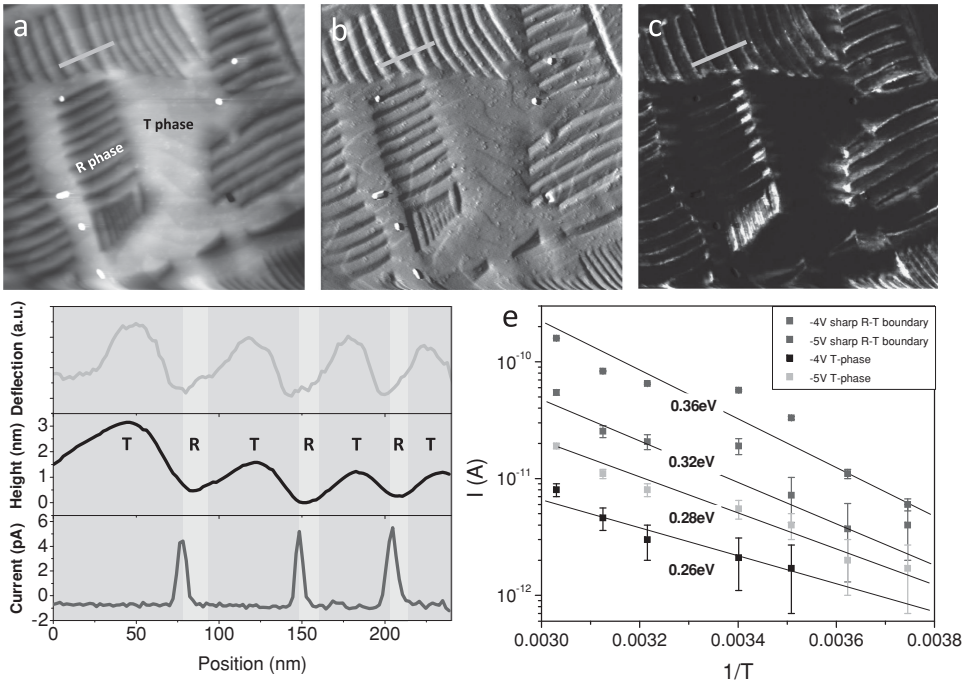

Figure 1. a) AFM topography of Ca-doped $BiFeO_3$, b) AFM deflection signal, c) conductive AFM current image, image size 3 micron, d) cross sections (at positions indicated by blue line in (a–c)) showing the correlation between the deflection signal (upper panel), topography (middle panel) and location of conducting features (bottom panel), e) temperature dependent c-AFM data and extracted activation energies for local conduction of sharp R–T boundary regions and pure T phase regions (two bias voltages shown for comparison).

revealing the position of the conductive feature in relation to the surface morphology. Clearly, the highest conductivity is found close to the steep side of the surface corrugation formed around the R-phase. In addition, the ends of the R-stripes show enhanced conduction coincident with the large curvature of the boundary (Figure 1c).[27] Temperature dependent measurements of the boundary conductivity are shown in summary in Figure 1e. As can be seen the conductivity is thermally activated for both boundary regions as well as the flat T-phase region. Absolute values for the activation energies lie in the 0.2–0.4 eV range. The differences in activation energy between the two are small of the order of 0.1 eV. Similar activation energies have been found for 109° ferroelectric domain walls in $BiFeO_3$.[31] The slightly higher activation energy of the boundary as compared to the bulk region (Figure 1e) is a feature that has been observed at 109° ferroelectric domain walls as well.

The mixed phase system has been attracting a lot of attention with the evidence of a strain driven morphotropic phase bondary[22] and the evidence of a large electrostrain[23] as the application of a local electric field results in the reversible phase transition from the (T) to the (R+T) phases. The capability to manipulate these phase boundaries, and its corresponding electronic properties, with electric field in the doped mixed phase to induce electrically conductive features was probed in **Figure 2**. The images give an example of the consequence

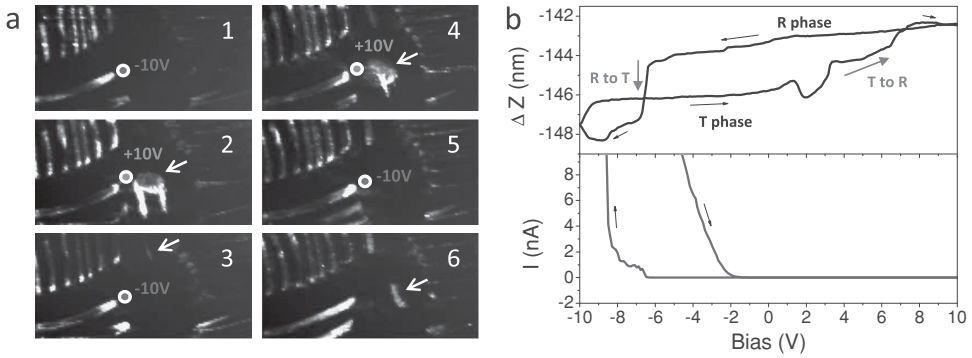

Figure 2. a) Local nanoscale phase transition between R- and T-phase induced by biased AFM tip and coupled creation / erasing of conductive R–T conductive boundaries. Red and blue dots indicate tip position for applied bias. b) Strain loop and simultaneous *I–V* curve showing correlation of nanoscale phase transition and local electronic conductivity. The *I–V* curve and strain loop were acquired simultaneously by placing the AFM tip on a conductive phase boundary and recording data during a bias voltage sweep.

of the electrostrain phenomenon on the conduction distribution. The red and blue dots in the images indicate the position where biases of +10V and –10V are applied, respectively. After the application of the local bias, increased conductivity is observed at a newly created R-phase boundary (arrows) at a different position (series in Figure 2a). While the dimension of the conductive tip is estimated to be 10–20 nm, the range of the observed non-locality is about one order of magnitude larger (100–200 nm). This effect is attributed to the local strain environment and its coupling to the field-induced local phase transition. This non-volatile conductive pattern can be erased after the application of the opposite bias polarity, evidencing the reversibility of the process. The correlation between local *I–V* curves and strain loops (Figure 2b) unveil the strong correlation between the phase transition and the occurrence of electronic conductivity variations. The phase transition between R and T phase can clearly be observed in the height change during the strain loop due to the large difference in c-axis parameter of the two phases. Upon creating local R-phase in a T area the local measured c-AFM current increases because phase boundaries are created, and the reverse process can be seen as well. Note, that the cycling of coupled creation / erasing processes seems not perfect and slightly different patterns are obtained in panel 2 and 4 of Figure 2a. We believe this is a very unusual finding and at the moment there is no direct application. However, the fact that a material can be influenced at one point in space and a change is seen at a different location some few hundred nanometers away is very intriguing, and we believe not very common. This effect might be interesting for example for non-local sensors and actuators that operate on the nanoscale.

In order to acquire deeper insight into the structure-conductivity relation, we performed combined HAADF-STEM and EELS studies of the various structural phases and boundaries, see **Figure 3**. The high quality HAADF image

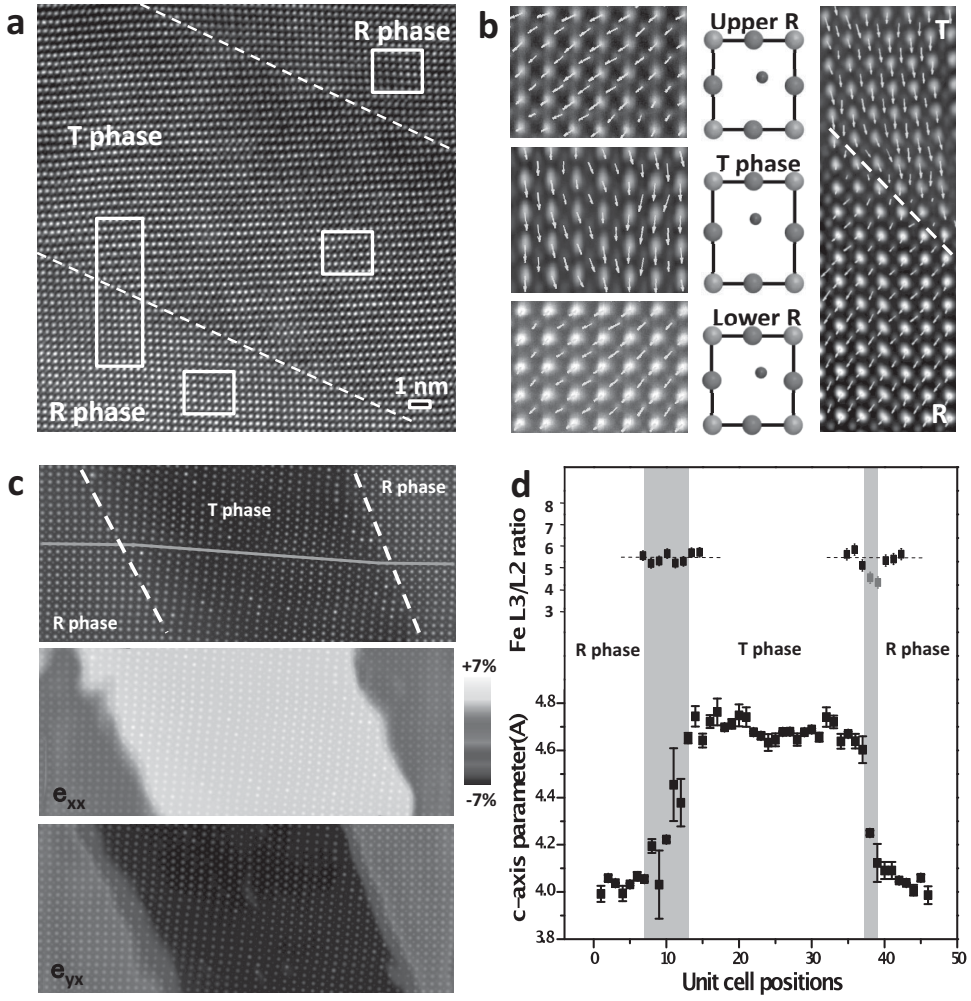

Figure 3. a) HAADF image of a region with mixed phases. The boundaries between R and T phases are indicated by dashed lines. Plot of the iron and bismuth displacement vectors D_{FB} for upper and lower R phases, T phase and the R-T interface are shown in (b). Both R phases have the same polarization orientation along the projection of electron beam direction. c,d) Asymmetric boundaries: structural analysis of the c-axis parameter reveals a "soft" 5 uc wide and a "sharp" 2 uc wide phase boundary. Blue line indicates profile position. In the insets the variation of Fe L3/L2 ratio is plotted as the probe is scanning across the R to T (soft) and T to R (sharp) boundary (R-T and T-R at the same common T area), respectively. Local strain changes ε_{xx} and ε_{yx} from peak pair analysis (PPA) using R-phase as reference are also shown indicating large strain gradients at the boundaries which result in altered octahedral tilts and bonding angles at the phase boundaries.

was obtained from the spherical aberration-corrected microscope (TEAM0.5). The structural R and T phases can readily be distinguished in the HAADF image and the local ferroelectric polarization vector can be assigned by the relative iron displacement vectors D_{FB}, which can be determined by fit as two-dimensional Gaussians and has a linear relationship with the projected polarization P_{YZ}.[35] The change of polarization from one phase to the other appears rather abrupt on the length scale of 2–5 unit cells (Figure 3d). Previous studies of the undoped material on the same substrate revealed the transition from structural variant R to T was occurring within a length of 10 unit cells.[22] Ca-doping therefore seems to lead to narrower phase boundaries. Interestingly, a strong asymmetry in the atomic structure of the boundary can be visualized. Our results show that the transition on opposite boundaries, i.e., from the same tetragonal grain to the next neighboring rhombohedral regions (from R–T and T–R) reveals both a "soft" 5 uc (unit cell) wide and a "sharp" 2 uc wide phase boundary (Figure 3d). This asymmetry was measured by HAADF-ST on several T domains showing that this is not a local effect, i.e., the phase boundary pairing seems universal in this material and is also reflected in the surface morphology (Figure 1). Especially the local AFM deflection signal shows this asymmetry as well and the local conductivity map reveals the sharp boundary exhibiting the largest currents (Figure 1d). Local strain changes ε_{xx} and ε_{yx} from peak pair analysis (PPA) using R-phase as reference are also shown in Figure 3c indicating large strain gradients (atomic distance changes) at the boundaries which result in altered octahedral tilts and bonding angles at the phase boundaries. A non-negligible difference in the strain gradient between the R to T and T to R interface is visible. In the present case, changes in oxygen octahedral tilt and changes in Fe–O–Fe bond angle lead to changed orbital mixing angles. The Fe–O–Fe angle is important because it controls both the magnetic exchange and orbital overlap between Fe 3d and O 2p orbitals, and as such it determines the magnetic ordering temperature and the conductivity of the material. The observed difference in conductivity at the phase boundaries (Figure 1) can then be attributed to local changes in the Fe–O–Fe angle. The pronounced asymmetry in phase boundary conductivity of the soft and sharp boundaries, suggests that the structural property of the interface, i.e., different local strain state and octahedral tilt play a more important role in the conductivity difference.[36–39] Thus, the exact nature of these phase boundaries determines the level of conductivity observed.[8,15,27]

Local EELS measurements operated in the probe corrected STEM mode are used to investigate the nanoscopic differences in electronic structure associated with the structural phase boundaries, see insets in Figure 3d. The fine structures of the Fe $L_{2,3}$ edges recorded from R-phase, T-phase, soft and sharp phase boundaries are shown (R-T and T-R at the same common T area). While no obvious change in chemical composition, e.g. local oxygen content, could be evidenced within the error bars of the measurement (see Supporting Information), the Fe L3/L2 ratio profiles show a variation depending on the probe position, thus clearly revealing a distinguished decrease at the phase boundaries when scanning along the sharp, i.e., more conducting interface (Figure 3d). Recent microscopy work[40] has shown the interplay between strain at the interface and octahedral tilt in $BiFeO_3$ thin film heterostructures. Furthermore, it has been discussed that boundary conductivity can be affected by the oxygen octahedral tilt.[36] We note that such structural changes are not accompanied with composition changes. In other words, the conductivity anisotropy could be attributed to local difference in octahedral tilt angles resulting from the dramatic changes in width of the interfacial regions.

In summary, we have shown that there is a strong correlation between the local strain state and the electronic properties at isosymmetric phase boundaries in mixed phase Ca-doped $BiFeO_3$ thin films. We clearly identify two types of phase boundary in this system: a sharp and a soft one. The strain gradient results in local oxygen environment changes causing the emergence of different activation energies and an anisotropic conductive pattern. This rather unusual electrically writable feature might find applications in nanotechnology where local bias application is not feasible and a remote, non-local switching is desirable. Furthermore, the recent discovery of enhanced ferromagnetism in highly strained BiFeO3 thin films with the magnetic moment lying along the needle's long axis suggest the high potential of this system for magnetoresistive nanoscale technologies.

Experimental Section

$BiFeO_3$ thin films doped with 2% Ca were grown on top of 10 nm thick $La_{0.5}Sr_{0.5}CoO_3$ epitaxial conductive electrode layers on $LaAlO_3$ substrates using pulsed laser deposition at 700 °C in 100 mTorr oxygen pressure. Typical deposition rates were approximately 2 nm min^{-1} with a laser repetition rate of 2 Hz. The pulsed KrF excimer laser with 248 nm was focused to reach a laser fluence of ≈1 J cm^{-2} on the target surface. The films were cooled down with the rate of 10 °C min^{-1} at ≈1 atm oxygen pressure. Ca-doping was chosen because it provides a way of controlling the defect structure in this material system, as oxygen vacancies are produced naturally in order to compensate calcium acceptors and maintain a highly stable Fe^{3+} valence state.[41–43] The crystal structure details of the Ca doped material as compared to the undoped material were determined by X-ray diffraction 2θ-ω scans (Panalytical X'Pert MRD Pro with Cu Kα1 radiation). The X-ray data shows the structural distortion of the R-phase, with out-of-plane lattice parameter of (c = 4.17 Å). From reciprocal space maps the in-plane dimensions of this highly strained R-phase are found to be 3.82 Å (for details see Supporting Information).

Supporting Information

Supporting Information is available from the Wiley Online Library or from the author.

Acknowledgements

The work at Berkeley is supported by the Director, Office of Science, Office of Basic Energy Sciences, Materials Sciences Division of the US Department of Energy under contract DE-AC02–05CH11231. J. S. acknowledges support by the Australian Research Council under grant numbers FT110100523, DP140100463, DP140102849 and by the National Research Foundation of Korea funded by the Korean Government (NRF-2013S1A2A2035418). T. U. and D. K. kindly acknowledge financial support by the RTG-DFG Project 1401. Work

at the Center for Nanophase Materials Sciences was performed in project CNMS2010–280, which is sponsored at Oak Ridge National Laboratory by the Scientific User Facilities Division, Office of Basic Energy Sciences, U.S. Department of Energy. Work at the University of Michigan was supported by the U.S. Department of Energy under award DE-FG02–07ER46416 and by NSF under awards DMR-0907191, DMR-0820404 and DMR-0723032 (aberration-corrected TEM instrument). We thank Cheuk-Wai Tai from Stockholm University for providing the PPA software.

Received: February 4, 2014
Revised: March 19, 2014
Published online: April 14, 2014

[1] G. Catalan, J. Seidel, R. Ramesh, J. F. Scott, *Rev. Mod. Phys.* **2012**, *84*, 119.
[2] P. Zubko, *Annu. Rev. Condens. Matter Phys.* **2011**, *2*, 141.
[3] J. Mannhart, D. G. Schlom, *Science* **2010**, *327*, 1607.
[4] D. M. Lind, S. D. Berry, G. Chern, H. Mathias, L. R. Testardi, *Phys. Rev. B.* **1992**, *45*, 1838.
[5] Y. Ijiri, J. A. Borchers, R. W. Erwin, P. J. van der Zaag, R. M. Wolf, *Phys. Rev. Lett.* **2007**, *99*, 147201.
[6] S.-Y. Yang, J. Seidel, S. J. Byrnes, P. Shafer, C.-H. Yang, M. D. Rossell, P. Yu, Y.-H. Chu, J. F. Scott, J. W. Ager, L. W. Martin, R. Ramesh, *Nat. Nanotechnol.* **2010**, *5*, 143.
[7] T. Choi, Y. Horibe, H. T. Yi, Y. J. Choi, W. Wu, S.-W. Cheong, *Nat. Mater.* **2010**, *9*, 253.
[8] D. Meier, J. Seidel, A. Cano, K. Delaney, Y. Kumagai, M. Mostovoy, N. A. Spaldin, R. Ramesh, M. Fiebig, *Nat. Mater.* **2012**, *11*, 284.
[9] V. Gopalan, V. Dierolf, D. A. Scrymgeour, *Annu. Rev. Mater. Res.* **2007**, *37*, 449.
[10] E. K. H. Salje, H. L. Zhang, *Phase Trans.* **2009**, *82*, 452.
[11] E. K. H. Salje, *Chem. Phys. Chem.* **2010**, *11*, 940.
[12] M. Schröder, A. Haußmann, A. Thiessen, E. Soergel, T. Woike, L. M. Eng, *Adv. Funct. Mater.* **2012**, *22*, 3936.
[13] W. Eerenstein, T. T. M. Palstra, S. S. Saxena, T. Hibma, *Phys. Rev. Lett.* **2002**, *88*, 247204.
[14] Y.-H. Shin, I. Grinberg, I.-W. Chen, A. M. Rappe, *Nature* **2007**, *449*, 881.
[15] J. Seidel, L. W. Martin, Q. He, Q. Zhan, Y. H. Chu, A. Rother, M. Hawkridge, P. Maksymovych, S. Kalinin, S. Gemming, P. Yu, N. Balke, M. Gajek, F. Wang, G. Catalán, J. F. Scott, N. A. Spaldin, J. Orenstein, R. Ramesh, *Nature Mater.* **2009**, *8*, 229.
[16] J. Seidel, *J. Phys. Chem. Lett.* **2012**, *3*, 2905.
[17] S. Farokhipoor, B. Noheda, *Phys. Rev. Lett.* **2011**, *107*, 127601.
[18] Y.-P. Chiu, Y.-T. Chen, B.-C. Huang, M.-C. Shih, J.-C. Yang, Q. He, C.-W. Liang, J. Seidel, Y.-C. Chen, R. Ramesh, Y.-H. Chu, *Adv. Mater.* **2011**, *23*, 1530.
[19] A. Lubk, S. Gemming, N. A. Spaldin, *Phys. Rev. B* **2009**, *80*, 104110.
[20] A. Lubk, M. D. Rossell, J. Seidel, Q. He, S. Y. Yang, Y. H. Chu, R. Ramesh, M. J. Hÿtch, E. Snoeck, *Phys. Rev. Lett.* **2012**, *109*, 047601.
[21] A. Lubk, M. Rossell, J. Seidel, Y.-H. Chu, R. Ramesh, M. Hÿtch, E. Snoeck, *Nano Lett.* **2013**, *13*, 1410.
[22] R. J. Zeches, M. D. Rossell, J. X. Zhang, A. J. Hatt, Q. He, C.-H. Yang, A. Kumar, C. H. Wang, A. Melville, C. Adamo, G. Sheng, Y.-H. Chu, J. F. Ihlefeld, R. Erni, C. Ederer, V. Gopalan, L. Q. Chen, D. G. Schlom, N. A. Spaldin, L. W. Martin, R. Ramesh, *Science* **2009**, *326*, 977.
[23] J. Zhang, B. Xiang, Q. He, J. Seidel, R. Zeches, P. Yu, S.-Y. Yang, C.-H. Yang, Y.-H. Chu, L. W. Martin, A. M. Minor, R. Ramesh, *Nat. Nanotechnol.* **2011**, *6*, 98.
[24] H. M. Christen, J. H. Nam, H. S. Kim, A. J. Hatt, N. A. Spaldin, *Phys. Rev. B* **2011**, *83*, 144107.
[25] C.-H. Yang, D. Kan, I. Takeuchi, V. Nagarajan, J. Seidel, *Phys. Chem. Chem. Phys.* **2012**, *14*, 15953.
[26] J. X. Zhang, Q. He, M. Trassin, W. Luo, D. Yi, M. D. Rossell, P. Yu, L. You, C. H. Wang, C. Y. Kuo, J. T. Heron, Z. Hu, R. J. Zeches, H. J. Lin, A. Tanaka, C. T. Chen, L. H. Tjeng, Y.-H. Chu, R. Ramesh, *Phys. Rev. Lett.* **2011**, *107*, 147602.
[27] P. Maksymovych, J. Seidel, Y.-H. Chu, A. Baddorf, P. Wu, L.-Q. Chen, S. V. Kalinin, R. Ramesh, *Nano Lett.* **2011**, *11*, 1906.
[28] J. Guyonnet, I. Gaponenko, S. Gariglio, P. Paruch, *Adv. Mater.* **2011**, *23*, 5377.
[29] P. Mokrý, A. K. Tagantsev, J. Fousek, *Phys. Rev. B* **2007**, *75*, 094110.
[30] E. A. Eliseev, A. N. Morozovska, G. S. Svechnikov, V. Gopalan, V. Y. Shur, *Phys. Rev. B* **2011**, *83*, 235313.
[31] J. Seidel, P. Maksymovych, A. J. Katan, Y. Batra, Q. He, A. P. Baddorf, S. V. Kalinin, C.-H. Yang, J.-C. Yang, Y.-H. Chu, E. K. H. Salje, H. Wormeester, M. Salmeron, R. Ramesh, *Phys. Rev. Lett.* **2010**, *105*, 197603.
[32] J. Seidel, D. Fu, S.-Y. Yang, E. Alarcòn-Lladò, J. Wu, R. Ramesh, J. W. Ager, *Phys. Rev. Lett.* **2011**, *107*, 126805.
[33] J. Seidel, S.-Y. Yang, E. Alarcòn-Lladò, J. W. Ager, R. Ramesh, *Ferroelectrics* **2012**, *433*, 123.
[34] J. Seidel, G. Singh-Bhalla, Q. He, S.-Y. Yang, Y.-H. Chu, R. Ramesh, *Phase Trans.* **2013**, *86*, 53.
[35] T. Nelson, B. Winchester, Y. Zhang, S.-J. Kim, A. Melville, C. Adamo, C. M. Folkman, S.-H. Baek, C.-B. Eom, D. G. Schlom, L.-Q. Chen, X. Pan, *Nano Lett.* **2011**, *11*, 828.
[36] G. Catalan, *Ferroelectrics* **2012**, *433*, 65.
[37] D. Wang, E. K. H. Salje, S.-B. Mi, C.-L. Jia, L. Bellaiche, *Phys. Rev. B* **2013**, *88*, 134107.
[38] S. Van Aert, S. Turner, R. Delville, D. Schryvers, G. Van Tendeloo, E. K. H. Salje, *Adv. Mater.* **2012**, *24*, 523.
[39] Y. Kim, M. Alexe, E. K. H. Salje, *Appl. Phys. Lett.* **2010**, *96*, 032904.
[40] Y.-M. Kim, A. Kumar, A. Hatt, A. N. Morozovska, A. Tselev, M. D. Biegalski, I. Ivanov, E. A. Eliseev, S. J. Pennycook, J. M. Rondinelli, S. V. Kalinin, A. Y. Borisevich, *Adv. Mater.* **2013**, *25*, 2497.
[41] C.-H. Yang, J. Seidel, S. Y. Kim, P. B. Rossen, P. Yu, M. Gajek, Y.-H. Chu, L. W. Martin, M. B. Holcomb, Q. He, P. Maksymovych, N. Balke, S. V. Kalinin, A. P. Baddorf, S. R. Basu, M. L. Scullin, R. Ramesh, *Nat. Mater.* **2009**, *8*, 485.
[42] J. Seidel, W. Luo, S. J. Suresha, P.-K. Nguyen, A. S. Lee, S.-Y. Kim, C.-H. Yang, J. Pennycook, S. T. Pantelides, J. F. Scott, R. Ramesh, *Nat. Comm.* **2011**, *3*, 799.
[43] J. Schiemer, R. Withers, L. Norén, Y. Liu, L. Bourgeois, G. Stewart, *Chem. Mater.* **2009**, *21*, 4223.